Experimental profile evolution of a high-density field-reversed configuration

E. L. Ruden
Air Force Research Laboratory, Directed Energy Directorate, 3550 Aberdeen Avenue SE, Kirtland AFB, New Mexico, 87117–5776

Shouyin Zhang, T. P. Intrator, and G. A. Wurden
Los Alamos National Laboratory, Los Alamos, New Mexico 87545

(Received 7 April 2006; accepted 30 October 2006; published online 18 December 2006)

A field-reversed configuration (FRC) gains angular momentum over time, eventually resulting in an $n=2$ rotational instability (invariant under rotation by π) terminating confinement. To study this, a laser interferometer probes the time history of line integrated plasma density along eight chords of the high-density ($\sim 10^{17}$ cm^{-3}) field-reversed configuration experiment with a liner. Abel and tomographic inversions provide density profiles during the FRC's azimuthally symmetric phase, and over a period when the rotational mode has saturated and rotates with a roughly fixed profile, respectively. During the latter part of the symmetric phase, the FRC approximates a magnetohydrodynamic (MHD) equilibrium, allowing the axial magnetic-field profile to be calculated from pressure balance. Basic FRC properties such as temperature and poloidal flux are then inferred. The subsequent two-dimensional $n=2$ density profiles provide angular momentum information needed to set bounds on prior values of the stability relevant parameter α (rotational to ion diamagnetic drift frequency ratio), in addition to a view of plasma kinematics useful for benchmarking plasma models of higher order than MHD. © *2006 American Institute of Physics*.
[DOI: 10.1063/1.2402130]

I. INTRODUCTION

The Field Reversed Configuration (FRC) eXperiment with a Liner (FRX-L) (Refs. 1 and 2), at present, forms and confines an FRC within a D_2 gas prefilled fused quartz tube with an inner and outer radius of 5.25 and 5.47 cm, respectively, via four coordinated pulsed power circuits which impose various magnetic-field components. A detailed description of the FRC formation hardware and circuit is available elsewhere.[3] The FRC's midplane is diagnosed with a 0.633 μm He-Ne laser interferometer with a fanned array of eight chordal probes sensitive to the free-electron density integrated along each chord. Details of the interferometer's design, and calculation of the phase-shift versus time contribution from the FRC plasma, are the subjects of a complementary paper.[4] Corrections due to phase-shift contributions from acoustic vibration and refractive index changes within the fused quartz resulting from the discharge are discussed therein. All results presented in this paper are from a single representative shot (#3213) prefilled with D_2 gas at 50 mTorr, and its corresponding vacuum reference shot (#3205, without gas prefill), used here to measure the interferometer's acoustic response to the experiment's pulsed magnetic-field. The "main" magnetic-field (which reverses the initial bias field), preionization, bias, and cusp/mirror magnetic-field circuit capacitor bank charge voltages for this shot are 70, 30, 8.7, and 8.5 kV, respectively (for comparison with other published results). The initial magnetic bias current is triggered 137.8 μs before the main bank trigger. The main bank's associated crowbar switch is triggered 2.7 μs after its own trigger. These times correspond to the quarter-cycle rise times of the bias and main bank magnetic-fields, respectively. The high-frequency (250 kHz) preionization circuit is triggered 23 μs before the main bank. $t=0$ on the presented time scale corresponds to the onset of magnetic reversal exterior to the fused quartz tube, where it is measured directly.

Figure 1 plots the chordal probes' phase-shift contribution due to the FRC plasma, as inferred from the aforementioned data reduction.[4] It is reproduced here, along with basic background information about the experiment, to make this paper self-contained. B_0, the external magnetic-field B_z of the plasma shot recorded by a time-integrated B-dot probe just external to the fused quartz tube near the FRC midplane, is overlaid for reference. All eight probe beams intersect $c_k=30.6$ cm from the z axis after passing through the tube. The probe impact parameters (the distance of closest approach of chords $k=0,1,\ldots,7$ to the z axis) are

$$\{r_k,\ k=0,1,\ldots,7\} = \{0.0,0.7,1.8,2.4,2.9,3.5,3.7,4.1\}\ \text{cm}. \tag{1}$$

The phase-shift ϕ due to the FRC plasma is approximated by[5]

$$A\phi = \int_{\substack{\text{beam}\\ \text{path}}} n_e dl, \tag{2}$$

where n_e is the free-electron density distribution of the FRC plasma, dl is the increment of path length of the laser beam, and, with laser wavelength $\lambda_0=0.633$ μm, $A=5.61\times 10^{16}$ cm^2/rad.

The FRC is approximately azimuthally symmetric initially, permitting Abel inversion of the phase-shift data to determine $n_e(r,t)$, where r is the cylindrical radius. Two complementary Abel inversion techniques are used. One, de-

 © 2006 American Institute of Physics

Downloaded 18 Dec 2006 to 129.238.237.96. Redistribution subject to AIP license or copyright, see http://pop.aip.org/pop/copyright.jsp

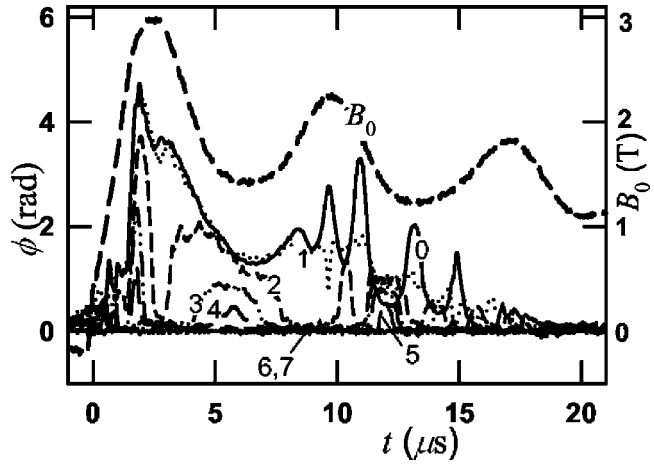

FIG. 1. The representative shot's phase-shift history for channels 0 through 7 (as labeled) with each channel's corresponding vacuum reference signal and wall phase-shift perturbation (based on chord 7) having been subtracted. B_0, the vacuum external B_z near the FRC midplane, is overlaid for reference. The traces for channels 6 and 7 are very small and difficult to distinguish.

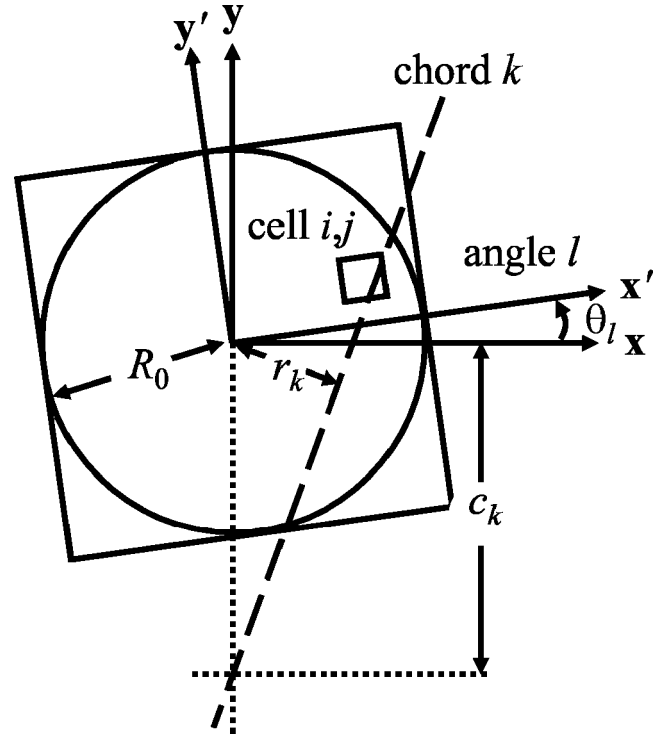

FIG. 3. Rotating square mesh used for tomographic inversion.

scribed in the first subsection of the Appendix, produces a result with a discontinuous gradient, but is fully consistent with the phase-shift data in the sense that line integration along the probed chords reproduces the original phase-shift data precisely. It is adequate for inferring spatially integrated properties such as mass and moment of inertia per axial unit length. The other method, based on an azimuthally symmetric application of the tomographic techniques described in the balance of the Appendix, produces a continuous function and gradient, with explicit weight given to reducing the characteristic magnitude of $\partial^2 n_e/\partial r^2$ to increase smoothness at the expense of spatial resolution. This is more suitable for quantifying n_e peaks and gradients needed for magnetohydrodynamic (MHD) equilibrium analysis from which basic FRC properties such as plasma temperature and poloidal flux are inferred.

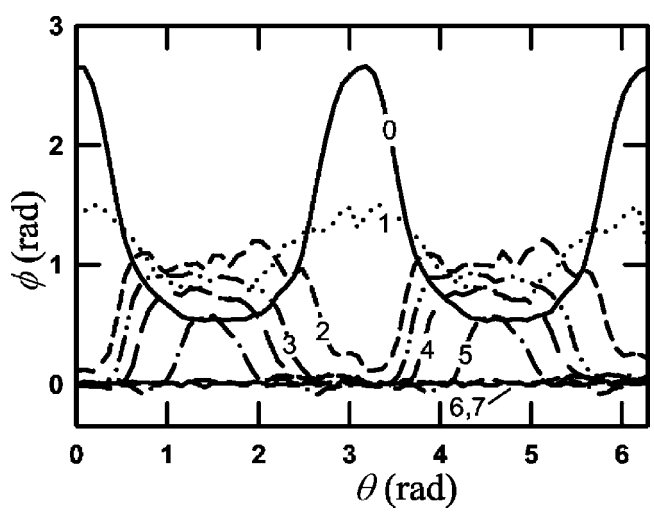

FIG. 2. Phase-shift ϕ for channels 0 through 7 after being corrected for vacuum response, wall effect, and an assumed uniform linear n_e decay between times $t=10.96$ μs and $t=13.20$ μs. These traces are assumed to result from an n_e distribution at $t=12.08$ μs of an FRC rotating about the tube axis at a constant rate from angle $\theta=0$ to π over the specified period due to a rotational instability with mode number $n=2$. The plot is then repeated to extrapolate it out to $\theta=2\pi$.

An FRC spontaneously gains angular momentum over time until $\alpha=\Omega_R/\Omega_{Di}$ reaches a critical value of order unity, at which time an instability with azimuthal mode number $n=2$ develops. Here, Ω_R and Ω_{Di} are the FRC's rotational and ion diamagnetic drift frequencies, respectively. The oscillations observed in Fig. 1 after $t=8$ μs are due to this instability. On experiments, such as FRX-L, this instability is observed to grow rapidly into a saturated state that appears to rotate with an n_e profile that varies slowly in the rotating frame except for a gradual overall decay. Figure 2 plots the decay corrected signals of Fig. 1 over a time interval interpreted as a uniform rotation by $2\pi/n$ using the procedure discussed in the second subsection of the Appendix. One can calculate from this the two-dimensional n_e distribution in the midplane of the saturated state since line integrated n_e versus time measurements taken along several chords of a rigidly rotating subject constitute a sufficient data set for tomographic inversion. The projection matrix for the rotating square mesh illustrated in Fig. 3, and the regularized inversion needed to calculate n_e, are the subjects of the third and fourth subsections, respectively, of the Appendix. "Regularization" involves imposing a characteristic scale length (smoothing) parameter L on the inferred n_e profile indicative of spatial resolution. Once the saturated n_e profiles are obtained, integrated properties such as mass and angular momentum per unit length in the axial direction are obtained for correlation with corresponding properties of the earlier azimuthally symmetric phase.

Downloaded 18 Dec 2006 to 129.238.237.96. Redistribution subject to AIP license or copyright, see http://pop.aip.org/pop/copyright.jsp

II. THEORETICAL CONSIDERATIONS

Given $n_e(r)$, B_0, and Ω_R, additional FRC properties such as the internal $B_z=B_z(r)$ profile, electron plus ion temperature $T=T_i+T_e$, and α may be inferred if we assume the FRC to approximate an axially invariant (highly prolate) rotational equilibrium with uniform Ω_R and T. Finding B_z and T for the azimuthally symmetric case in the MHD approximation, for example, entails subjecting the steady-state integrated form of the momentum equation,

$$B_z^2(r) = B_0^2 - 2\mu_0 n_e(r) k_B T - 2\mu_0 \Omega_R^2 m^* \int_r^{R_0} r' n_e(r') dr', \tag{3}$$

to the FRC constraints that $B_z=0$ and $\partial(B_z^2)/\partial r=0$ at some finite (B_z reversal) radius $r=R_1$. Here, m^* is the mass correlated with each electron (approximately the deuteron mass for our plasma) and $R_0=5.25$ cm is the inner radius of the fused quartz FRC tube. The second constraint ensures that the $B_z=0$ radius is also a local minimum of $B_z^2(r)$ (needed to keep B_z real everywhere). Eliminating T between the two equations that result from imposing the FRC constraints on Eq. (3) at $r=R_1$ gives

$$\left(B_0^2 - 2\mu_0 \Omega_R^2 m^* \int_r^{R_0} r' n_e(r') dr'\right) \frac{\partial n_e}{\partial r} - 2\mu_0 \Omega_R^2 m^* r n_e^2 = 0 \quad (r=R_1). \tag{4}$$

This may be solved numerically to obtain R_1. Substituting R_1 into Eq. (3) with $B_z^2=0$ then provides T. Substituting this T back into Eq. (3) then provides $B_z(r)$. In the limiting case of $\Omega_R=0$, $r=R_1$ occurs at the peak of $n_e(r)$, and T may be found by solving Eq. (3) with $n_e(r)=n_e(R_1)$ and $B_z^2=\Omega_R=0$ for it directly. $n_e \sim 5\times 10^{16}$ cm^{-3} and $T\sim 200$ eV for the results presented, so the thermal equilibration time for our (deuterium) plasma is ~ 1.3 μs (Ref. 6). This is sufficiently short for our purposes to assume $T_i=T_e=T/2$ in later calculations in this paper.

Ω_R may be determined directly for the saturated $n=2$ mode from the frequency of the ϕ modulation recorded by the interferometer (Fig. 1). Estimating Ω_R during the azimuthally symmetric phase, though, is more difficult. Given $B_z(r)$, area integration provides an estimate of the axial flux Φ_l threading the midplane interior to $r=R_l=5.63$ cm, which may be compared to a direct measurement of Φ_l by a flux loop at $r=R_l$ wrapped around the tube. The centripetal term in Eq. (3) shifts the n_e peak outward relative to R_1, having the net effect of increasing the B_z integrated Φ_l estimate as Ω_R increases for a given $n_e(r)$. Varying Ω_R until there is agreement with directly measured Φ_l, therefore, provides a self-consistent way to determine Ω_R *in principle*. Other processes, though, have at least as big of an effect as Ω_R on the difference between the two Φ_l estimates. Indeed, except for an interval of at most 3 μs, deviation from equilibrium beforehand, and from azimuthal symmetry afterwards (as the $n=2$ mode develops), results in a Φ_l discrepancy too big for the B_z profile to be considered meaningful regardless of the value of Ω_R assumed. As an alternative, an upper bound on Ω_R may be established by assuming that the mean angular momentum per unit mass within the midplane $\Omega_R r_{\rm rms}^2$ is conserved prior to $n=2$ mode saturation. Here, $r_{\rm rms}$ is the mean-squared radius of the n_e distribution calculated from the Abel and tomographic inversions. This only gives an upper bound since FRC angular momentum actually increases and particle number decreases with time. A lower bound on Ω_R (as argued in Sec. IV) is provided by assuming that $\Omega_R r_{\rm rms}^2$ increases in proportion to t up to $n=2$ mode saturation.

Estimates of the magnetic separatrix radius R_s and poloidal flux Φ_p may also be calculated directly from $B_z(r)$; R_s is the radius out to which the area integral of $B_z(r)$ from $r=0$ (interior axial flux) is zero, and Φ_p is the magnitude of the axial flux interior to $r=R_1$. Fortunately, these estimates are only weakly dependent on (poorly known) Ω_R. It is instructive to compare these estimates to commonly cited ones based on directly measured Φ_l and B_0 alone. R_s, for example, may be approximated by assuming that B_z is uniform between R_s and the main magnetic-field coil inner radius $R_c=6.20$ cm. This implies[7]

$$R_s = \sqrt{R_c^2 - \frac{\Phi_c}{\pi B_0}}, \quad \Phi_c = \Phi_l + \pi B_0 (R_c^2 - R_l^2), \tag{5}$$

where Φ_c is the flux interior to $r=R_c$ (extrapolated from the direct Φ_l measurement[8]). Referred to as the "excluded flux radius," a similar result (within a few percent) is obtained from the "multiloop method" discussed in the latter reference for our experiment. Φ_p, meanwhile, may be estimated from[9]

$$\Phi_p = \pi R_c^2 B_0 \left(\frac{R_s}{\sqrt{2} R_c}\right)^{3+\varepsilon}, \tag{6}$$

where Eq. (5) is used for R_s, and ε is a phenomenological parameter. If one assumes that there is no plasma pressure for $r>R_s$, $\varepsilon=0$ and $\varepsilon=1$ give upper and lower bounds on Φ_p, respectively.

Finding the midplane $B_z(x,y)$ profile for the subsequent saturated $n=2$ state is more complicated since it does not approximate an MHD equilibrium. Higher-order terms such as the finite Larmour radius (FLR) stress tensor are needed for a minimal description. The tomographic inversions at saturation, therefore, are ideally suited for testing extensions to MHD. Further advantages for this application are the FRC midplane cross section's wide range of magnetization, and unidirectional magnetic-field (which greatly simplifies the FLR stress tensor). Abel inversion during the symmetric phase alone is not a sensitive bench test since azimuthally symmetric FRC equilibria are describable approximately by MHD theory already, with higher-order terms affecting the radial profile in detail only. Even the coarsest features of the saturated $n=2$ instability, though, such as its radial elongation ratio, require an FLR treatment since MHD theory of a highly prolate FRC implies the radial elongation should increase until the plasma hits the wall. This is because rotational modes of an FRC are essentially Rayleigh-Taylor (R-T) in nature, but with acceleration being centripetal, and the R-T instability saturates with a finite expansion velocity in the MHD description.

For a simplified FLR treatment of the rotational instability, Roberts and Taylor[10] show that for the planar R-T case

Downloaded 18 Dec 2006 to 129.238.237.96. Redistribution subject to AIP license or copyright, see http://pop.aip.org/pop/copyright.jsp

where mass density ρ_0 increases with height as $\exp(\lambda x)$ in a gravitational field of acceleration g, R-T modes are stable for magnetically transverse wavenumbers k provided

$$g \leq \nu^2 \lambda k^2, \quad \nu = \frac{k_B T_i}{2ZeB}. \tag{7}$$

Here, ν is the "gyroviscosity" coefficient, with k_B, Z, e, and B being the Boltzmann constant, mean ionization level, elementary charge, and magnetic-field magnitude, respectively. To apply this result to a rotating FRC with an axial magnetic-field of characteristic magnitude B, note that the ion diamagnetic drift frequency is

$$\Omega_{Di} = -\frac{v_{Di}}{r}, \quad \mathbf{v}_{Di} = -\frac{\nabla p_i \times \mathbf{B}}{eZn_i B^2}, \tag{8}$$

where $\mathbf{v}_{Di}$ is the diamagnetic drift velocity, and p_i and n_i are the ion pressure and number density, respectively. Using centripetal acceleration for g at the characteristic radius R_1, and wrapping the mode "plane" around the circumference, we have then the characteristic values

$$\Omega_{Di} = \frac{2\lambda\nu}{R_1}, \quad g = \Omega_R^2 R_1, \quad k = \frac{n}{R_1}. \tag{9}$$

From Eq. (7), our stability criterion is then

$$\alpha = \frac{\Omega_R}{\Omega_{Di}} \leq \frac{n}{2\sqrt{\lambda R_1}}. \tag{10}$$

Given a characteristic density gradient scale length of $1/\lambda \approx R_1$, stability requires $\alpha \lesssim 1$ for the least stable mode $n=2$. Technically, $n=1$ goes unstable first, but the (planar) model applied to cylindrical geometry does not conserve lateral linear momentum for this mode, so is inapplicable. The threshold is respectably close to the threshold value observed[11] and described by more sophisticated modeling,[12–14] given the geometrical liberties taken. Taking further liberties to apply this description beyond the linear growth phase (for the purpose of hypothesis), $n=2$ saturation may be qualitatively described as the result of Ω_R decreasing to conserve angular momentum as the $n=2$ lobes radially expand until α falls below its instability threshold. Quantitatively, though, this hypothetical rotating fluid equilibrium state has never been described mathematically.

The dynamics of the $n=2$ mode is of particular concern for the magnetized target fusion[1,2] (MTF) application because α theoretically increases significantly during wall compression by a conducting cylindrical liner. To show this, firstly, Ω_R increases in proportion to R_s^{-2} from angular momentum conservation. Meanwhile, $x_s \equiv R_s/R_c$ is conserved during cylindrical wall compression, where R_c (in this context) is the liner inner radius (Tuszewski,[9] p. 2058). Given this, plasma β is conserved [Tuszewski, Eq. (10)]. Given *this* and flux conservation, Ω_{Di} is proportional to T_i [Shimamura and Nogi,[15] Eq. (7) with $\Omega^* = -\Omega_{Di}$]. The FRC's characteristic volume $V = \pi R_s^2 l_s$, meanwhile, decreases as R_s^N, where l_s is the separatrix length and N is the dimensionality of compression. Assuming adiabatic compression, $T_i V^{(5/3)-1}$ is conserved. Therefore, $\Omega_{Di} R_s^{2N/3} = \text{constant}$, and Ω_{Di} increases in proportion to $R_s^{-2N/3}$. α, then, increases in proportion to $R_s^{-2}/R_s^{-2N/3} = R_s^{-2(1-N/3)}$. $N=12/5$ for cylindrical wall compression (Tuszewski,[9] Table V), so α increases in proportion to $R_s^{-2/5}$ or, equivalently, $R_c^{-2/5}$. The (target) factor of 10 radial compression, then, increases α by a factor of $10^{2/5} \approx 2.5$.

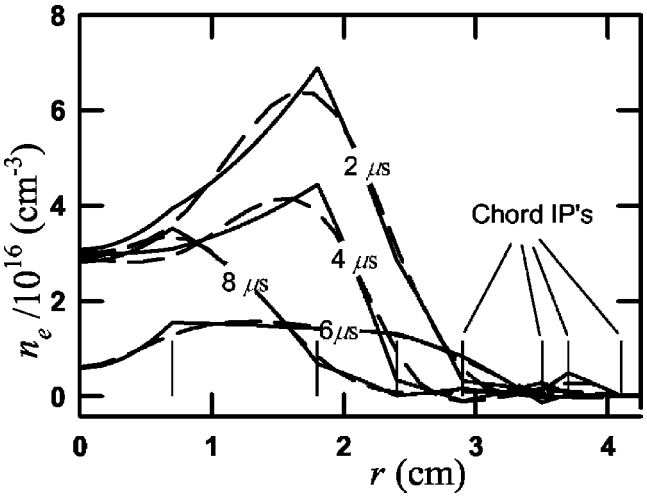

FIG. 4. Free-electron density n_e vs radius r at different (labeled) times of the representative shot from the Abel inversion algorithm presented in the first subsection of the Appendix (solid), and by instructing the tomographic algorithm that an $n=1$ mode rotates with a negligible period around the given times (dashed). The vertical lines are at the chordal impact parameter (IP) locations.

III. RESULTS

If the time interval $[t_{\min}, t_{\max}]$ assumed for a $2\pi/n$ rotation is too brief for any significant variation in the phase-shift data $\{\phi_k(t),\ k=0,1,\ldots,q-1\}$ to occur, where k is the probe index and q is the number of probes, the tomographic inversion algorithm will produce an azimuthally symmetric n_e profile. That is, an Abel inversion will effectively result. This fact is used to test the algorithm's function by comparing n_e profiles produced in this way to those of the Abel inversion algorithm in the first subsection of the Appendix, as plotted in Fig. 4. For this, we assume an $n=1$ mode rotates with a negligible period (1 ns) at the labeled times, with excellent agreement. For these inversions, as with all that follow, a $p \times p = 51 \times 51$ mesh is used, the fixed n_e profile FRC construction is "sampled" at $s=71$ different angles, and $L=0.5$ cm is assigned. The resultant distributions are suitable for calculating gradients for the MHD equilibrium analysis, and provide a convenient visualization of the effect of characteristic scale length L described in the fourth subsection of the Appendix.

Figure 5 plots the n_e distribution of the representative shot inferred from $\{\phi_k(\theta)\}$ plotted in Fig. 2, which assumes $n=2$. That is, the $q=8$ functions are sampled at $s=71$ angles θ, and used to define the $sq=568$ elements of column vector $\mathbf{\Phi}$ for use in Eq. (A28). Figure 6 illustrates how the FRC is inferred to have evolved after the next π rotation bounded by the peaks in ϕ_0 (diameter probe) at $t_{\min}=13.20$ μs and $t_{\max}=14.90$ μs.

Figure 7 plots the principle distribution moment Λ_0 and mean squared radius r_{rms} [defined by and following Eq.

Downloaded 18 Dec 2006 to 129.238.237.96. Redistribution subject to AIP license or copyright, see http://pop.aip.org/pop/copyright.jsp

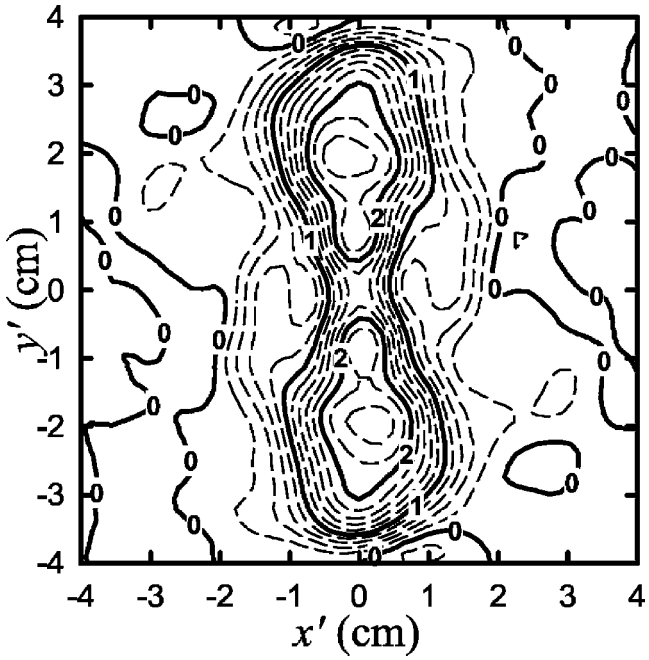

FIG. 5. n_e from tomographic inversion for the representative shot assuming an $n=2$ mode rotates by π between the peaks in ϕ_0 at 10.96 and 13.20 μs, based on the corrected data plotted in Fig. 2. This profile best represents the FRC at 12.08 μs. Major contour labels are in units of 10^{16} cm^{-3}.

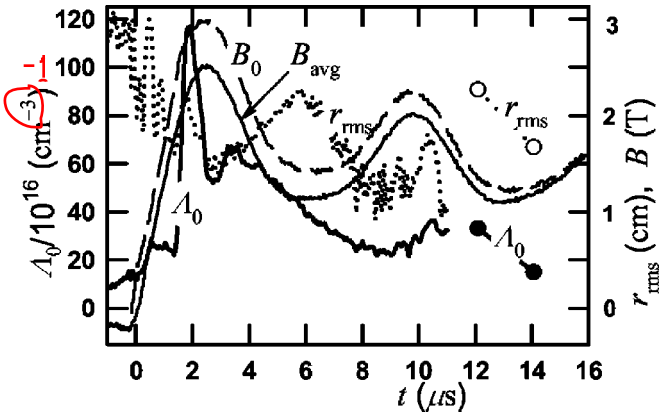

FIG. 7. Λ_0 and r_{rms} [defined by and following Eq. (A7)] based on the Abel inversion of the data plotted in Fig. 1 using the algorithm described in the first subsection of the Appendix (continuous curves) followed by the discrete values calculated from Eq. (A29) for the tomographic inversions of Figs. 5 and 6 at their respective representative times. Vacuum external B_z near the FRC midplane B_0 and $B_{avg} \equiv \Phi_l/(\pi R_l^2)$, based on axial flux Φ_l measured by a loop of radius $r=R_l$, are compared to illustrate the diamagnetic effect of the FRC.

(A7)] based on the Abel inversion of the corrected data plotted in Fig. 2 using the algorithm of the first subsection in the Appendix (continuous curves) followed by the discrete values calculated from Eq. (A29) for the tomographic inversions of Figs. 5 and 6. The discrete times are taken to be the oscillation midpoints of the signals used to obtain the tomographic inversions. As with Fig. 1, B_0 is overlaid for reference.

Figures 8 and 9 plot n_e if we assume that the first time interval used for Fig. 5 is due instead to an $n=1$ mode, with the midplane density centroid orbiting the z axis, or an $n=3$ mode, respectively. Both assumed mode numbers result in significant negative n_e artifacts.

Abel inversions using the tomographic algorithm are used to infer B_z versus r based on the isothermal MHD equilibrium solution of Eq. (3) subject to the FRC condition of

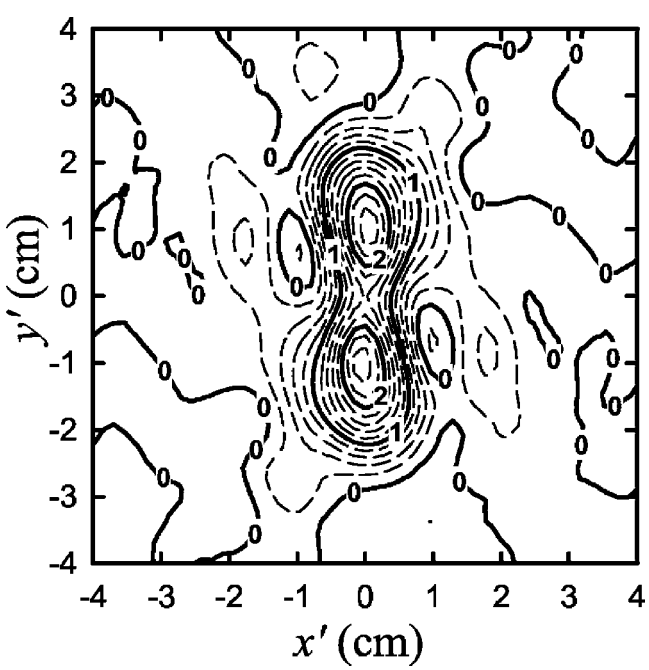

FIG. 6. n_e from tomographic inversion assuming an $n=2$ mode rotates by π between the peaks in ϕ_0 at 13.20 and 14.90 μs (see Fig. 1), representing the FRC at $t=14.05$ μs. Note the disappearance of the prominent outer lobes. Major contours are at 10^{16} cm^{-3} intervals.

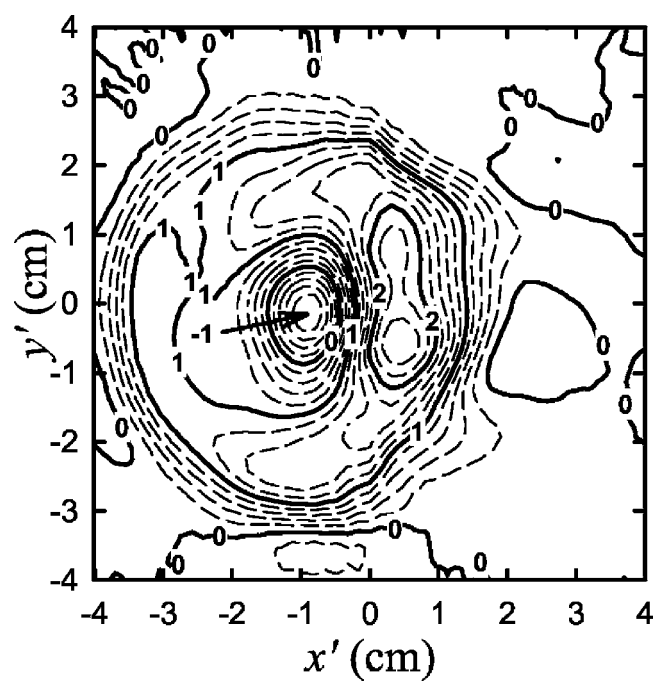

FIG. 8. n_e from tomographic inversion assuming an $n=1$ mode rotates by 2π between 10.96 and 13.20 μs. Note the physically meaningless negative n_e peak of amplitude -1.0×10^{16} cm^{-3} [labeled "**−1**" near $(x',y')=(-1,0)$ cm]. Major contours are at 10^{16} cm^{-3} intervals.

Downloaded 18 Dec 2006 to 129.238.237.96. Redistribution subject to AIP license or copyright, see http://pop.aip.org/pop/copyright.jsp

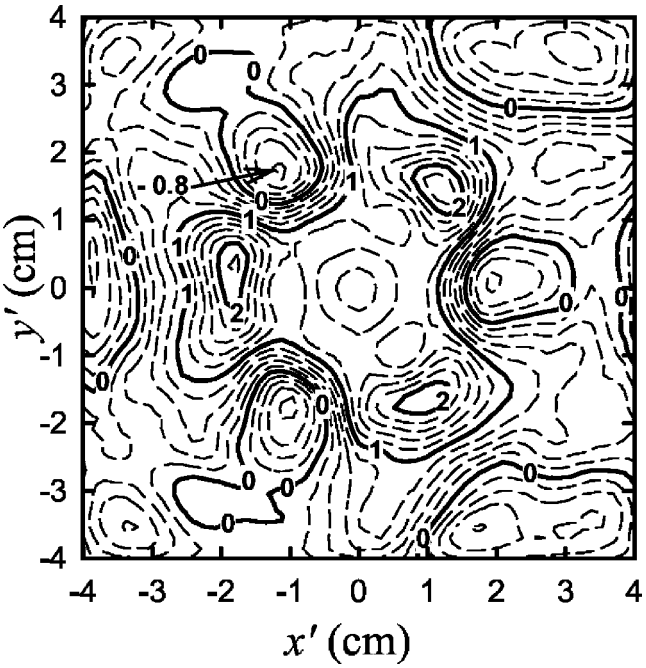

FIG. 9. n_e from tomographic inversion assuming an $n=3$ mode rotates by $2\pi/3$ between 10.96 and 13.20 μs. Note the three physically meaningless negative n_e peaks of amplitude -0.8×10^{16} cm^{-3} that lay between the three positive lobes. Major contours are at 10^{16} cm^{-3} intervals.

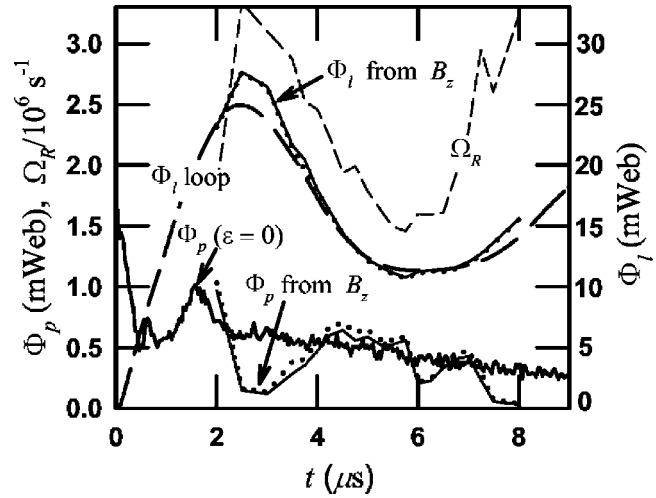

FIG. 11. Comparative estimates of axial and poloidal flux Φ_l and Φ_p, respectively. Φ_l is measured directly with a flux loop (dashed line), and from B_z integration based on the FRC solution to Eq. (3) for $\Omega_R=0$ (dotted) and for Ω_R as plotted (solid). The Ω_R plot (thin dashed) assumes angular momentum conservation per unit mass up to the first tomographic inversion of the $n=2$ instability (Fig. 5), where it can be determined accurately. The Φ_l plots are reasonably consistent with each other from $t=4$ μs to $t=7$ μs. Φ_p is likewise estimated from B_z integration assuming $\Omega_R=0$ (dotted) and the aforementioned Ω_R (solid) for comparison with the upper bound ($\varepsilon=0$) of Eq. (6) (solid line with high-frequency noise). The latter is based on directly measured B_0 and Φ_l only.

Eq. (4). Figure 10 plots the results for a range of times for the case of $\Omega_R=0$. Figure 11 plots the MHD solution's axial flux Φ_l interior to $r=R_l$, and poloidal flux Φ_p for $\Omega_R=0$ and for the Ω_R time history plotted. $\Omega_R(t)$ here is chosen to conserve the mean angular momentum per particle $\Omega_R r_{\rm rms}^2$ up to the tomographic inversion representative of the FRC at $t=12.08$ μs (Fig. 5). Independent estimates of Φ_l and Φ_p based on a flux loop at $r=R_l$ and the upper limit of Eq. (6) ($\varepsilon=0$), respectively, are overlaid for comparison. An alternate representation of measured Φ_l is plotted in Fig. 7, here divided by the flux loop area for comparison with B_0, to better illustrate the relative magnitude of axial flux exclusion by the FRC.

Figure 12 plots the time histories of various other properties of interest for the nonrotating and $\Omega_R r_{\rm rms}^2$ conserving B_z profiles. The separatrix radius R_s based on Eq. (5) (excluded flux radius) is plotted for comparison with that calcu-

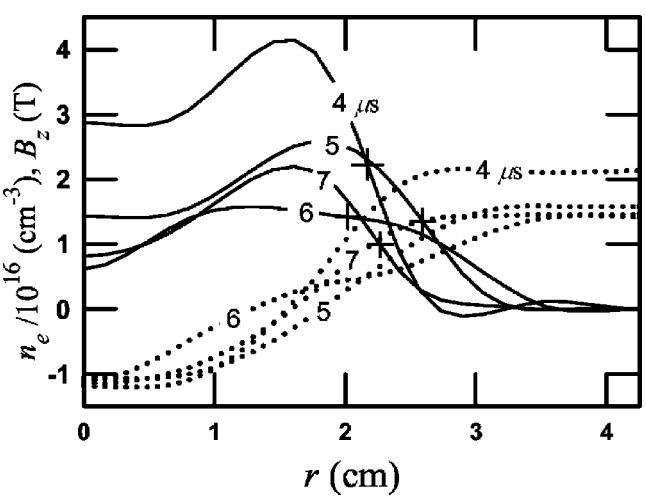

FIG. 10. B_z vs r (dotted lines) for a range of times (labeled) based on the tomographic algorithm-based Abel inversions n_e (solid lines) assuming an isothermal, z invariant, azimuthally symmetric FRC in MHD equilibrium [Eq. (3) with FRC condition Eq. (4)] with angular velocity $\Omega_R=0$. The inferred separatrix radius $r=R_s$ is marked with a "+" on the corresponding n_e plots. The "+" near the crossing point of the n_e curves for $t=4$ μs and $t=5$ μs belongs to the $t=4$-μs curve.

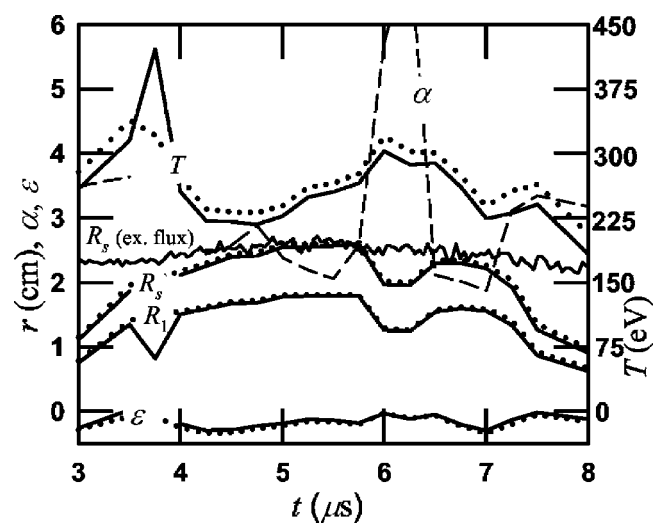

FIG. 12. Various properties of the FRC solution to B_z in Eq. (3) (MHD equilibrium) with $\Omega_R=0$ (dotted) and Ω_R as plotted in Fig. 11 (solid). The separatrix radius R_s based on Eq. (5) (excluded flux radius) is plotted (with high-frequency noise) for comparison. R_1 is the magnetic null radius, $T=T_i+T_e$, and $\alpha=\Omega_R/\Omega_{Di}$, where Ω_{Di} [Eq. (8)] is solved at the MHD solution's separatrix and assumes $T_i=T_e=T/2$. The plotted ε is solved from Eq. (6), but with Φ_p and R_s based on area integration of the B_z solution.

Downloaded 18 Dec 2006 to 129.238.237.96. Redistribution subject to AIP license or copyright, see http://pop.aip.org/pop/copyright.jsp

lated from B_z. The ε curve plotted is taken to be Eq. (6) solved for this parameter, but with Φ_p and R_s based on the MHD solution to B_z. $\alpha=\Omega_R/\Omega_{Di}$ is also plotted, where Ω_{Di} [Eq. (8)] is solved at the MHD solution's separatrix assuming $T_i=T/2$. For the other plots, R_1 is the magnetic null radius and $T=T_i+T_e$.

IV. DISCUSSION

The moments $\{\Lambda_i\}$ defined by Eq. (A7) are of the midplane n_e profile only, since this is the only place where n_e data is presently available. Although these numbers provide useful direct metrics for correlation with computer simulations, any inferences about global properties, such as total particle load and moment of inertia, require assumptions about the axial distribution of the FRC. Fortunately, the $r_{\rm rms}^2=\Lambda_1/\Lambda_0$ (used for estimating bounds on Ω_R versus t) *is* representative of the entire FRC. The observation that the axial distribution of excluded flux radius[16] estimate of R_s does not vary greatly for this experiment due to confining (mirror) magnetic-field coils on opposite ends of the FRC is also fortunate. The FRC length at half max of R_s remains 20 ± 4 cm between the maximum and minimum of the of B_0 oscillations, based on an axial array of external B_z measurements.[2] Without the mirror coils, the FRC length would oscillate more significantly with B_0.

Although the Abel inversion derived portion of the results represented in Fig. 7 is plotted out to $t=11$ μs, it appears from Fig. 1 that the $n=2$ instability (which breaks the azimuthal symmetry assumed) starts to grow at $t=8$ μs. This is evident from the fact that the lower two chords increase while the higher ones decrease, indicating that the $n=2$ lobes are swinging into the vertical position (out of view of the higher chords). Accuracy beyond that time for Abel inversion cannot be expected, as suggested by the erratic oscillations in $r_{\rm rms}$ after 8 μs. More detailed correlations discussed below suggest an even earlier onset. The Abel inversion implies a steady drop in Λ_0 from 4 μs until up to 8 μs, then, presumably due the FRC losing particles. Over this same interval, $r_{\rm rms}$ tracks the FRC expanding radially then recompressing in response to the fall and second rise of B_0, respectively. Λ_0 appears to stabilize between 8 μs and the first tomography based Λ_0 estimate at $t=12$ μs. This suggests that the rate of particle loss during this interval is low despite the radial growth of the $n=2$ mode, as quantified by the large jump in $r_{\rm rms}$ at 12 μs. This interval coincides with the second peaking of B_0. Radial compression due to a rising B_0 has been implicated in destabilizing the $n=2$ mode (which indeed starts growing significantly during this interval) in an already spinning FRC because of a resultant increase in Ω_R as $r_{\rm rms}$ decreases due to angular momentum conservation.[17] Decreasing the oscillation amplitude of the B_z during this time (as has been achieved in more recent shots[18]) may mitigate this effect.

The tomographic images provide insight into the basic dynamics by which the FRC loses mass after the $n=2$ instability has grown to its greatest extent at 12 μs. Comparing Fig. 5 to Fig. 6 suggests that the plasma loses about 2/3 of its remaining mass over a rotation by π after instability saturation from the outer lobes (which contain most of the mass at that point), leaving a relatively undisturbed core behind. The overall dumbbell-shaped cross section is corroborated by and complements a similar pattern observed in tomographic inversions of an FRC's bremsstrahlung emission density.[19] The physically meaningless negative n_e regions that appear in the tomographic inversions that assume $n=1$ and $n=3$, as shown in Figs. 8 and 9, respectively, provide further corroboration that the mode number is indeed $n=2$. This result was unanticipated since n is a formal (albeit well established) *assumption* of the inversion. An important caveat, however, is that the $n=1$ tilt mode (where the FRC rotates about an axis normal to the z axis), is *not* precluded by these inversions since this mode mimics $n=2$ for midplane n_e profiles. That is, the midplane n_e distribution of the tilt mode is invariant under a rotation by π (like $n=2$). The strongest justification that the mode is $n=2$, therefore, remains with prior work, such as that cited in the second subsection of the Appendix.

While the Abel inversion algorithm of the first subsection in the Appendix is suitable for calculating integrated properties of FRC such as its moments, Abel inversions based on the tomographic algorithm (which gives explicit weight to smoothing spatial dependencies) are more suitable for the B_z calculations since local properties such as gradients and peaks of n_e are needed. The resultant B_z profiles assume an isothermal azimuthally symmetric axially invariant equilibrium describable by MHD. However, the equilibrium assumption is invalid for early times since FRC formation is dynamic, and the azimuthally symmetric assumption breaks down as the $n=2$ instability develops. Comparing the area integral of the B_z solution out to $r=R_l$ to an independent measurement of Φ_l by a conducting loop at that radius provides a consistency check of the assumptions. The sensitivity of this test is enhanced by the fact that an error in the FRC's poloidal flux Φ_p is amplified by about of factor of $2\sqrt{2}$ in its effect on Φ_l since poloidal magnetic-field lines pass through the midplane twice, and the plasma has $\beta\sim1$. This amplification is important since, as one sees from Fig. 11, $\Phi_l\sim30\Phi_p$. From Fig. 11, then, the B_z solution can only be expected to be representative of the FRC for, at most, 4 μs $\lesssim t\lesssim 7$ μs. That is why only this time range is spanned in Fig. 10. Even within this range, the Φ_l discrepancy from the loop measurement is at times more than the amount that the B_z integration inferred Φ_l increases when going from $\Omega_R=0$ to its $\Omega_R r_{\rm rms}^2$ conserved value. For example, $\Omega_R=3.9\times10^6$ s^{-1} is required to bring B_z inferred Φ_l up to its directly measured value at $t=5.75$ μs, when the former falls furthest below the latter if rotation is neglected. And, at times when the nonrotating B_z integration inferred Φ_l is *greater* than its directly measured value, no real value of Ω_R leads to a match.

$\Omega_R r_{\rm rms}^2$ only provides an upper bound on Ω_R because of the FRC's angular moment gain and particle loss over time. For comparison, $\Omega_R=2.5\times10^6$ s^{-1} is implied if we assume that ϕ_0 peaks plotted in Fig. 1 at $t=8.38$ μs and $t=9.64$ μs bound a rotation by π during the early stages of $n=2$ growth. This is about 30% lower than one would expect from the $\Omega_R r_{\rm rms}^2$ conserved plot of Fig. 11 at $t\simeq8$ μs. According to

Downloaded 18 Dec 2006 to 129.238.237.96. Redistribution subject to AIP license or copyright, see http://pop.aip.org/pop/copyright.jsp

hybrid FRC simulations,[14] though, the real modulation frequency ω_r can be tens of percent lower than $2\Omega_R$ (indicative of an $n=2$ perturbation rotating in phase with the plasma), at least while the perturbation is at low amplitude (before the saturated lobes sweep up the plasma). $\Omega_R=2.5\times10^6$ s^{-1}, then, is only a *lower bound* on Ω_R at this time. Since the tomographic inversion that establishes the upper bound on $\Omega_R r_{\rm rms}^2$ occurs at $t\simeq12$ μs, this is (more or less) consistent with $\Omega_R r_{\rm rms}^2$ increasing in proportion to t. Lacking better data, this will be our lower bound estimate of $\Omega_R r_{\rm rms}^2$. This bound can be supported on physical grounds too. A leading theory for the cause of spin-up is the preferred opposing angular moment of particles migrating across the separatrix.[20] The Λ_0 plot of Fig. 7, meanwhile, implies that the rate of particle loss decreases significantly for later times up to $n=2$ mode saturation. This suggests that a linear rise in $\Omega_R r_{\rm rms}^2$ falls below the actual time history. Since the FRC profile is perturbed only slightly by rotation, the lower bound on α would then be $t/(12\ \mu\text{s})$ times its $\Omega_R r_{\rm rms}^2$ conserving upper bound.

Agreement between the B_z profile estimate of Φ_p (which is insensitive to Ω_R) with the upper bound expected based on Eq. (6) is reasonably good, except for a curious dip peaked around $t=6.2$ μs. This dip coincides with a significant fattening of the FRC (see the $r_{\rm rms}$ plot of Fig. 7 or the n_e at $t=6$ μs plot of Fig. 10) correlated with a local minimum in (the radially confining) B_0. Since there is no apparent mechanism for Φ_p to recover by $t=7$ μs, the most likely explanation is that this is an artifact of one of the assumptions of the B_z profile being violated. A corresponding dip appears in the R_s plot of Fig. 12 based on B_z integration, when it falls well below the excluded flux radius. The latter (based only on direct measurements of B_0 and Φ_l) is more accurately interpreted as a measure of $\sqrt{A_s/\pi}$, where A_s is the cross-sectional area where open magnetic-field lines are excluded (azimuthally symmetric or otherwise). Interpreted as such, the only significant assumption it requires is that plasma pressure exterior to this area is negligible. A real FRC, though, continuously loses particles across the separatrix (where they eventually escape along open magnetic-field lines). If our B_z profile were accurate, R_s inferred therefrom should only be about $\sim10\%$ lower than the excluded flux radius since Fig. 10 indicates that there is only about this much of the FRC mass exterior to R_s. A good explanation for the dip is lacking, although one possibility is that the $n=2$ mode is already of significant amplitude during at $t=6$ μs. Further planned experiments which involve a magnetic-field crowbar circuit with significantly less oscillation and more optimally spaced impact parameters may help resolve this issue.

Preceding the present analysis, and guided by previous FRX-series data, Eq. (6) with $\varepsilon=0.25$ has been used in published FRX-L estimates of Φ_p (Ref. 2). $\varepsilon=0$ is used instead for the Eq. (6) based Φ_p plot of Fig. 11 because (except for the dip) it agrees with our B_z profile based estimate better. To illustrate this, ε is calculated by substituting our B_z profile's Φ_p and R_s time histories into Eq. (6) and solving for it directly. The result is plotted in Fig. 12. This plot actually results in ε slightly less than zero. This can be accounted for by the fact that, as with the excluded flux radius, Eq. (6) neglects plasma pressure beyond $r=R_s$. $\varepsilon=0$ results in a value of Φ_p about 37% higher than $\varepsilon=0.25$, given our $R_s/R_c\approx0.4$.

Figure 12 only plots α at $r=R_s$ to conserve space. α does vary with r, but it is found for our results that its separatrix value is fairly representative of the FRC in the outer region. At $t=7$ μs, for example, around the time the $n=2$ instability appears to commence, α ramps down gradually from $\alpha=2.4$ at $r=1.75$ cm to $\alpha=1.4$ at $r=2.6$ cm, with the plotted value of $\alpha=1.9$ at $r=R_s=2.4$ cm being close to the mean in this range. α has a highly exaggerated response to the dip in R_s (Fig. 12) around $t=6$ μs due to $\partial n_e/\partial r$ being so small at $r=R_s$ then (Fig. 10). This further suggests that one or more assumptions of the MHD solution are compromised during the dip. If, as suggested, the $n=2$ mode actually starts before the dip, the upper bound on the critical α for stability remains unchanged since $\alpha\approx2$ then, too. Our best guess as to the lower bound before the dip (about halfway to the first $n=2$ inversion) is then $\alpha\approx1$.

V. SUMMARY AND CONCLUSIONS

The n_e profiles presented, and properties derivable therefrom, provide insight and quantitative information relevant to the basic dynamics of the FRC. Tomographic profiles of the saturated $n=2$ instability provide an important benchmark for direct comparison with future extended MHD or hybrid simulations. Prospects for improving $n=2$ rotational instability behavior by reducing B_z oscillations are suggested. Abel inversions provide the basis for estimating critical FRC properties such as n_e, Φ_p, and T indicating that Φ_p is near its maximum theoretical value consistent with external Φ_l and B_0 measurements. Broad bounds on stability relevant parameter α are established consistent with that reported elsewhere ($1\leq\alpha\leq2$). A method to improve the accuracy of the α estimate based on MHD (or higher order theory) rotational equilibrium profile consistency with an external Φ_l measurement is suggested, pending more accurate data.

ACKNOWLEDGMENTS

The authors would like to acknowledge W. J. Waganaar, R. Renneke, and D. Begay for FRX-L operations, and I. G. Furno for advice on numerical methods.

APPENDIX: INVERSION ALGORITHMS

1. Symmetric phase Abel inversion

The plasma is nominally azimuthally symmetric before the $n=2$ instability starts to develop, permitting n_e to be inferred by Abel inversion. The following algorithm derived here is computationally efficient and fully consistent with the ϕ data input. From Eq. (2),

$$A\phi(w)=\int_w^{R_0^2} n_e(s)\frac{1}{\sqrt{s-w}}ds, \tag{A1}$$

where the n_e is assumed to be zero for cylindrical radius

Downloaded 18 Dec 2006 to 129.238.237.96. Redistribution subject to AIP license or copyright, see http://pop.aip.org/pop/copyright.jsp

$r > R_0$ (generally the fused quartz tube's inner radius), ϕ is expressed here as a continuous function of the impact parameter squared w, and $s = r^2$.

Our measurements consist of $\phi(w)$ for q discrete chords with impact parameters $\{r_k,\ k=0,1,\ldots,q-1,\ r_{k+1} > r_k\}$.

$$w_k = r_k^2, \quad \phi_k = \phi(w_k), \quad k = 0,1,\ldots,q-1. \tag{A2}$$

The Abel inversion algorithm presented results in $n_e(s)$ being solved for at radii equal to the impact parameters for each of these chords,

$$n_k = n_e(w_k), \quad k = 0,1,\ldots,q-1. \tag{A3}$$

Since Abel inversion necessarily assumes that $n_e = 0$ beyond $r = R_0$, we add an artificial chord q (not actually probed) corresponding to

$$r_q = R_0, \quad w_q = R_0^2, \quad \phi_q = n_q = 0. \tag{A4}$$

There is no unique solution to $\{n_k\}$ consistent with $\{\phi_k\}$ measurements for finite q. There is, however, a unique solution to $n_e(s)$, and therefore $\{n_k\}$, where $n_e(s)$ is *defined* as the piecewise linear fit between points $\{w_k, n_k\}$,

$$n_e(s) = \left(\frac{n_{k+1} - n_k}{w_{k+1} - w_k}\right)s + \left(\frac{n_k w_{k+1} - n_{k+1} w_k}{w_{k+1} - w_k}\right)$$
$$w_k \le s \le w_{k+1}. \tag{A5}$$

The above provides an algorithm (after some series manipulations) to find $\{n_k,\ k=0,1,\ldots,q-1\}$ versus $\{r_k,\ k=0,1,\ldots,q-1\}$ recursively. In order of performance,

$$\begin{aligned}
&\{r_k, \phi_k, \quad k = 0,1,\ldots,q-1\},\\
&r_q = R_0, \quad \phi_q = n_q = 0,\\
&w_k = r_k^2, \quad k = 0,1,\ldots,q,\\
&\left(\frac{n_{q-1}}{A}\right) = \frac{3\phi_{q-1}}{4\sqrt{w_q - w_{q-1}}},\\
&S_{kj} = \frac{(w_k + 2w_j - 3w_{k-1})\sqrt{w_k - w_j}}{(w_k - w_{k-1})} + \frac{2(w_{k-1} - w_j)\sqrt{w_{k-1} - w_j}}{(w_k - w_{k-1})}\\
&\quad + \frac{(w_k + 2w_j - 3w_{k+1})\sqrt{w_k - w_j}}{(w_{k+1} - w_k)}\\
&\quad + \frac{2(w_{k+1} - w_j)\sqrt{w_{k+1} - w_j}}{(w_{k+1} - w_k)},\\
&\left(\frac{n_j}{A}\right) = \frac{3\phi_j - 2\sum_{k=j+1}^{q-1}\left(\frac{n_k}{A}\right)S_{kj}}{4\sqrt{w_{j+1} - w_j}} \quad \text{for } j = q-2, q-3, \ldots, 0.
\end{aligned} \tag{A6}$$

Equation (A5), then, gives $n_e(s)$. Note that $n_e(s)$ calculated in this manner is the algorithm's unique solution, and that $\{r_k, n_k\}$ are merely reference points. It reproduces the original data precisely upon Abel integration [Eq. (A1)], but results in parabolic lines connecting points $\{r_k, n_k\}$ if n_e is plotted versus r, with first derivative discontinuities where they meet. Although there are an infinite number of other solutions to $n_e(r)$ consistent with the data in this sense, other interpolation schemes connecting $\{r_k, n_k\}$ will, in general, not be.

Having obtained $\{n_k,\ k=0,1,\ldots,q\}$ from Eq. (A6), Eq. (A5) may be used to calculate the i'th moment $(i=0,1,\ldots)$ of n_e defined as

$$\Lambda_i \equiv \int_{\substack{\text{cross}\\ \text{section}}} n_e r^{2i} da = \pi \sum_{k=0}^{q-1}$$
$$\left[\frac{n_{k+1} - n_k}{w_{k+1} - w_k}\frac{w_{k+1}^{2+i} - w_k^{2+i}}{2+i} + \frac{n_k w_{k+1} - n_{k+1} w_k}{w_{k+1} - w_k}\frac{w_{k+1}^{1+i} - w_k^{1+i}}{1+i}\right], \tag{A7}$$

where da is the increment of area. $m^*\Lambda_0$, $m^*\Lambda_1$, and $r_{\text{rms}}^2 = \Lambda_1/\Lambda_0$, then, are the mass and the moment of inertia for rotations about the z axis per unit axial length at the FRC midplane, and the mean squared radius there, respectively.

2. Saturated $n=2$ mode assumptions

A single fanned array of chords does not provide a sufficient data set to determine the n_e profile at the midplane without additional assumptions. While Abel inversion assumes azimuthal symmetry, for the rotational instability we assume that the FRC rotates at a constant rate, that its n_e distribution remains constant in the rotating frame except for a scale factor that decreases linearly with time, and that after this "droop correction" the profile is invariant under a rotation by $2\pi/n$, where n is the integer mode number. Measurements taken at numerous times, then, may be interpreted as the fanned array probing the FRC at numerous angles. This provides a sufficient data set for tomographic inversion.

Mode $n=2$ is assumed based on previous research which shows that $n=2$ is dominant, as revealed by end on imaging,[9,21] and on theoretical analyses.[12–14] It has been demonstrated by diameter probing interferometry elsewhere[22] that the characteristic interferometric oscillations in ϕ_0 of Fig. 1 after $t=8$ μs are the signature of the $n=2$ mode. Although there is not yet any compelling direct empirical evidence that $n=2$ is the dominant mode for FRX-L specifically, inversions performed assuming $n=1$ and $n \ge 3$ result in significant regions of inferred negative n_e, and are, therefore, physically meaningless.

The decay rate is determined from the amplitude of the first chord (0) at $t=t_{\min}$ and at $t=t_{\max}$, the beginning and end of a period of signal oscillation, respectively, from peak to peak. $\{\phi_k(t),\ k=0,1,\ldots,q-1\}$ are multiplied by a linear function of t so that the amplitude for chord 0 at $t=t_{\min}$ and $t=t_{\max}$ is the average of $\phi_0(t_{\min})$ and $\phi_0(t_{\max})$. This assumption is justified by the near periodic nature of the phase-shift signals during the time interval corresponding to the instability after it has "saturated," or grown to its maximum spatial extent. The inversion is presumed to be representative of the FRC at the midpoint of this sampling period.

The droop corrected phase-shift for chord k when the FRC is rotated by angle $\theta = \theta_l = 2\pi l/s$, $l=0,1,\ldots,s-1$, is then

$$\phi_{k,l} = (At_l + B)\phi_k(t_l - m(t_{\max} - t_{\min}))$$

Downloaded 18 Dec 2006 to 129.238.237.96. Redistribution subject to AIP license or copyright, see http://pop.aip.org/pop/copyright.jsp

$$\text{for} \quad t_{\min} \le t_l - m(t_{\max} - t_{\min}) < t_{\max},$$
$$m = 0, 1, \ldots, n-1, \tag{A8}$$
$$t_l = t_{\min} + (t_{\max} - t_{\min}) nl/s.$$

Here, t_l is the time the idealized FRC construction is at angle θ_l (extrapolated beyond $t = t_{\max}$ up to a full rotation), and s is the effective number of angles the construction is sampled at.

A and B are determined by requiring continuity of the droop corrected ϕ_0 after rotation by $2\pi/n$,

$$(At_{\min} + B)\phi_0(t_{\min}) = (At_{\max} + B)\phi_0(t_{\max}), \tag{A9}$$

and by requiring ϕ_{00} (the initial droop corrected phase-shift for chord for chord 0) to be the mean of the two peak amplitudes $\phi_0(t_{\min})$ and $\phi_0(t_{\max})$,

$$(At_{\min} + B)\phi_0(t_{\min}) = \frac{\phi_0(t_{\min}) + \phi_0(t_{\max})}{2}. \tag{A10}$$

Solving for the coefficients,

$$A = \frac{[\phi_0(t_{\min}) + \phi_0(t_{\max})][\phi_0(t_{\min}) - \phi_0(t_{\max})]}{2\phi_0(t_{\min})\phi_0(t_{\max})(t_{\max} - t_{\min})},$$
$$B = \frac{\phi_0(t_{\min}) + \phi_0(t_{\max})}{2\phi_0(t_{\min})}\left(1 - \frac{[\phi_0(t_{\min}) - \phi_0(t_{\max})]t_{\min}}{\phi_0(t_{\max})[t_{\max} - t_{\min}]}\right). \tag{A11}$$

Figure 2 plots the resultant droop corrected phase-shift plots derived from the first fully developed oscillation of Fig. 1.

3. Mesh and projection matrix

The droop corrected n_e distribution is assumed to be constant in reference frame (x', y') rotating about the z axis, as illustrated in Fig. 3. (x, y) are the coordinates of the stationary frame. We impose a rotating p by p cell square grid mesh centered on the z axis of side length $2R_0$, where R_0 is the radius outside of which n_e is assumed to be zero. For numerical efficiency, $R_0 = r_{q-1}$ (the highest impact parameter) is used here (instead of the fused quartz tube inner radius). For $(i = 0, 1, \ldots, p-1,\ j = 0, 1, \ldots, p-1)$, (x', y') is within cell (i, j) if, and only if

$$x'_i \le x' < x'_{i+1}, \quad x'_i = (2i/p - 1)\ R_0,$$
$$y'_j \le y' < y'_{j+1}, \quad y'_j = (2j/p - 1)\ R_0. \tag{A12}$$

Note that x' and y' indices go up to p since p columns (rows) have $p+1$ boundaries. The line integral of n_e is sampled along q stationary chords with the plasma at s different angles in the range $0 \le \theta < 2\pi$. n_e is assumed uniform within each cell.

Given our mesh assumptions, Eq. (2) may be represented by

$$A\Phi_w = \sum_{u=0}^{p^2-1} M_{u,w} N_u,$$
$$w = 0, 1, \ldots, qs - 1, \tag{A13}$$

where $\Phi_{lq+k} = \phi_{k,l}$, $M_{jp+i,lq+k}$ is the length of the portion of chord k within cell (i, j) when the plasma is at angle l ($M_{jp+i,lq+k} = 0$ if the chord misses the cell), and N_{jp+i} is n_e in cell (i, j).

For use in calculating $\{M_{u,w}\}$, the equation describing chord k in the (stationary) $x-y$ plane is

$$x = a_k(y + c_k), \quad a_k = \frac{r_k}{\sqrt{c_k^2 - r_k^2}}, \tag{A14}$$

where r_k is the chord k's impact parameter, and c_k is the distance between the z axis and the point where chord k crosses the y axis. In terms of the rotating coordinates,

$$x = x' \cos\theta - y' \sin\theta,$$
$$y = x' \sin\theta + y' \cos\theta. \tag{A15}$$

So, in the rotating frame, the chord is described by

$$x'(\cos\theta - a_k \sin\theta) = y'(a_k \cos\theta + \sin\theta) + a_k c_k. \tag{A16}$$

From this, the intersection of chord k with the line $y' = y'_j$ when the plasma is at angle at l occurs at $x' = X_{j,k,l}$, where

$$X_{j,k,l} = \frac{y'_j(a_k \cos\theta_l + \sin\theta_l) + a_k c_k}{\cos\theta_l - a_k \sin\theta_l}. \tag{A17}$$

Likewise, the intersection of chord k with the line $x' = x'_i$ at plasma angle l occurs at $y' = Y_{i,k,l}$, where

$$Y_{i,k,l} = \frac{x'_i(\cos\theta_l - a_k \sin\theta_l) - a_k c_k}{a_k \cos\theta_l + \sin\theta_l}. \tag{A18}$$

The criteria for deciding if chord k passes through any two of the four sides of the cell (i, j) (L, T, R, and B for left, top, right, and bottom, respectively, in the rotated frame) at angle l (six possible ways), and the resultant value of $M^2_{jp+i,lq+k}$ (from the Pythagorean theorem) are

$$Y_{i,k,l} \ge y'_j \ \&\ Y_{i,k,l} < y'_{j+1} \ \&\ X_{j+1,k,l} \ge x'_i \ \&\ X_{j+1,k,l} < x'_{i+1}$$
$$(L\ \&\ T) \to M^2_{jp+i,lq+k} = (X_{j+1,k,l} - x'_i)^2 + (y'_{j+1} - Y_{i,k,l})^2,$$
$$Y_{i,k,l} \ge y'_j \ \&\ Y_{i,k,l} < y'_{j+1} \ \&\ Y_{i+1,k,l} \ge y'_j \ \&\ Y_{i+1,k,l} < y'_{j+1}$$
$$(L\ \&\ R) \to M^2_{jp+i,lq+k} = (x'_{i+1} - x'_i)^2 + (Y_{i+1,k,l} - Y_{i,k,l})^2,$$
$$Y_{i,k,l} \ge y'_j \ \&\ Y_{i,k,l} < y'_{j+1} \ \&\ X_{j,k,l} \ge x'_i \ \&\ X_{j,k,l} < x'_{i+1}$$
$$(L\ \&\ B) \to M^2_{jp+i,lq+k} = (X_{j,k,l} - x'_i)^2 + (Y_{i,k,l} - y'_j)^2,$$
$$X_{j+1,k,l} \ge x'_i \ \&\ X_{j+1,k,l} < x'_{i+1} \ \&\ Y_{i+1,k,l} \ge y'_j \ \&\ Y_{i+1,k,l} < y'_{j+1} \tag{A19}$$
$$(T\ \&\ R) \to M^2_{jp+i,lq+k} = (x'_{i+1} - X_{j+1,k,l})^2 + (y'_{j+1} - Y_{i+1,k,l})^2,$$
$$X_{j+1,k,l} \ge x'_i \ \&\ X_{j+1,k,l} < x'_{i+1} \ \&\ X_{j,k,l} \ge x'_i \ \&\ X_{j,k,l} < x'_{i+1}$$
$$(T\ \&\ B) \to M^2_{jp+i,lq+k} = (X_{j+1,k,l} - X_{j,k,l})^2 + (y'_{j+1} - y'_j)^2,$$

Downloaded 18 Dec 2006 to 129.238.237.96. Redistribution subject to AIP license or copyright, see http://pop.aip.org/pop/copyright.jsp

$$Y_{i+1,k,l} \geq y'_j \;\;\&\;\; Y_{i+1,k,l} < y'_{j+1} \;\;\&\;\; X_{j,k,l} \geq x'_i \;\;\&\;\; X_{j,k,l} < x'_{i+1}$$

$$(R \;\&\; B) \rightarrow M^2_{jp+i,lq+k} = (x'_{i+1} - X_{j,k,l})^2 + (Y_{i+1,k,l} - y'_j)^2,$$
$$\text{otherwise} \quad M^2_{jp+i,lq+k} = 0.$$

4. Regularized least-squares-fit solution

Equation (A13) is, in matrix notation,

$$A\mathbf{\Phi} = \mathbf{MN}, \quad \mathbf{\Phi} \in \mathbb{R}^{sq},$$
$$\mathbf{M} \in \mathbb{R}^{p^2 \times sq}, \quad \mathbf{N} \in \mathbb{R}^{p^2}. \tag{A20}$$

The order of the matrix element column and row indices u and w, respectively, in Eq. (A13) is reversed relative to the usual convention. This is done to make the notation consistent with the indexing order used by programming language IDL™, which is used to perform the tomographic analysis. There is, in general, a unique solution to $\mathbf{N}$ only for $p^2 = qs$. The problem is generally underspecified or overspecified if $p^2 < qs$ or $p^2 > qs$, respectively. Even for $p^2 = qs$, though, the exact solution is found to be dominated by numerical artifacts of high spatial frequency.

Tomographic inversion is, instead, accomplished by minimizing the χ^2 deviation of the corrected phase-shift measurements from the line integrated inferred n_e profile quantified on the rotating square mesh *plus* a second-order linear "regularizing" term[23] proportional to the spatially integrated square of the finite-element Laplacian magnitude of n_e. The latter term is needed to avoid high spatial frequency artifacts. This means minimizing

$$\frac{\|\mathbf{MN} - A\mathbf{\Phi}\|^2}{sq} + L^6 \frac{\|\mathbf{\Delta N}\|^2}{p^2} \quad \mathbf{\Delta} \in \mathbb{R}^{p^2 \times p^2}. \tag{A21}$$

Here, the term on the left is the χ^2 deviation of the phase-shift measurement that would result from the proposed meshed solution from the corrected phase-shift measurement itself. The term on the right is a second-order regularizing function quantifying the spatially integrated noise level of the solution, with $\mathbf{\Delta}$ being a finite-element matrix representation of the Laplacian operator acting on $\mathbf{N}$. L is a positive real parameter that increasingly suppresses the noise level of the solution as it is increased. It is taken to the sixth power so as to have the same unit of distance used to measure the mesh. This parametrization is chosen [as opposed to $\alpha = sqL^6/(2p^2)$ of Anton[23]] since L may be interpreted as a measure of the characteristic scale length of n_e variations of the solution. Spatial resolution is generally difficult to predict precisely in tomography, but L is closely correlated to it. In practice, L's value is chosen somewhat subjectively so as to give physically reasonable results. Selecting an L value roughly equal to the typical impact parameter separation, for example, results in a reasonable solution to $\mathbf{N}$ with low spatial frequency.

Our finite-element representation of the Laplacian of n_e in the vicinity of cell (i,j) is

$$(\mathbf{\Delta N})_u = \sum_{u'=0}^{p^2-1} \Delta_{u'u} N_{u'}, \tag{A22}$$

where $u = jp + i$. To determine the elements of $\mathbf{\Delta}$, the following characteristic values of $\partial^2 n_e / \partial x'^2$ and $\partial^2 n_e / \partial y'^2$ near cell (i,j) are taken to be those of the quadratic fits to $\{(x'_{i-1}, N_{jp+i-1}), (x'_i, N_{jp+i}), (x'_{i+1}, N_{jp+i+1})\}$ at $y' = y'_i$ and $\{(y'_{i-1}, N_{(j-1)p+i}), (y'_i, N_{jp+i}), (y'_{i+1}, N_{(j+1)p+i})\}$ at $x' = x'_i$, respectively,

$$\left(\frac{\partial^2 n_e}{\partial x'^2}\right)_{ij} = \frac{p^2(N_{jp+i-1} - 2N_{jp+i} + N_{jp+i+1})}{4R_0^2},$$
$$\left(\frac{\partial^2 n_e}{\partial y'^2}\right)_{ij} = \frac{p^2(N_{(j-1)p+i} - 2N_{jp+i} + N_{(j+1)p+i})}{4R_0^2}. \tag{A23}$$

Elements with out-of-range subscripts are assumed to be equal to zero. We then take the sum of these two terms to be $(\mathbf{\Delta N})_{jp+i}$. One may then verify the following by substituting it into Eq. (A22):

$$\Delta_{u'u} = \frac{p^2}{4R_0^2}(\delta_{u'+1,u} - 2\delta_{u'u} + \delta_{u'-1,u} + \delta_{u'+p,u} - 2\delta_{u',u} + \delta_{u'-p,u}), \tag{A24}$$

where δ is the Kronecker delta.

The minimum of expression (A21) is the solution to[23]

$$\left(\mathbf{M}^{\mathrm{T}}\mathbf{M} + \frac{sqL^6}{2p^2}\mathbf{\Delta}^{\mathrm{T}}\mathbf{\Delta}\right)\mathbf{N} = A\mathbf{M}^{\mathrm{T}}\mathbf{\Phi}, \tag{A25}$$

where superscript T means transpose ($\mathbf{\Delta}^{\mathrm{T}} = \mathbf{\Delta}$ in our representation, incidentally). A numerically stable solution may be obtained by the singular value decomposition (SVD) method.[24,25] From this, we obtain the SVD of the term in parentheses in Eq. (A25),

$$\left(\mathbf{M}^{\mathrm{T}}\mathbf{M} + \frac{sqL^6}{2p^2}\mathbf{\Delta}^{\mathrm{T}}\mathbf{\Delta}\right) = \mathbf{UWV}^{\mathrm{T}},$$
$$\mathbf{U} \in \mathbb{R}^{p^2 \times sq}, \quad \mathbf{W} \in \mathbb{R}^{p^2 \times p^2}, \quad \mathbf{V} \in \mathbb{R}^{p^2 \times p^2}, \tag{A26}$$

where $\mathbf{U}$ and $\mathbf{V}$ are orthogonal, and $\mathbf{W}$ is a diagonal matrix with nonnegative elements,

$$\mathbf{U}^{\mathrm{T}}\mathbf{U} = \mathbf{I}, \quad \mathbf{V}^{\mathrm{T}}\mathbf{V} = \mathbf{VV}^{\mathrm{T}} = \mathbf{I},$$
$$\mathbf{W} = \mathrm{diag}(w_1, \ldots, w_{p^2-1}), \quad w_{i+1} \geq w_i. \tag{A27}$$

$\mathbf{I}$, here, is the $p^2 \times p^2$ identity matrix. The solution to Eq. (A25) is

$$\mathbf{N} = A\mathbf{VW}^{-1}\mathbf{U}^{\mathrm{T}}\mathbf{M}^{\mathrm{T}}\mathbf{\Phi},$$
$$\mathbf{W}^{-1} = \mathrm{diag}(w_0^{-1}, \ldots, w_{p^2-1}^{-1}). \tag{A28}$$

Per method, if any of the $\{w_i\}$ values are zero (or, in practice, very small), the corresponding diagonal element of $\mathbf{W}^{-1}$ is set to zero.

Downloaded 18 Dec 2006 to 129.238.237.96. Redistribution subject to AIP license or copyright, see http://pop.aip.org/pop/copyright.jsp

Operations on **N** may be used to calculate the n_e distribution's radial moments and gradient components as needed. The k'th moment, defined by Eq. (A7), may be approximated by

$$\Lambda_k = 2\pi \int_{-R_0}^{R_0} \int_{-R_0}^{R_0} (x'^2 + y'^2)^k n_e dx' dy' \approx 2\pi \left(\frac{2R_0}{p}\right)^2 \sum_{j=0}^{p-1} \sum_{i=0}^{p-1} N_{jp+i} \left[\left(x_i' + \frac{R_0}{p}\right)^2 + \left(y_j' + \frac{R_0}{p}\right)^2 \right]^k, \tag{A29}$$

where the effect of finite cell size on Λ_1 has been neglected. Elements of matrix operators $\boldsymbol{\nabla}_{x'}$ and $\boldsymbol{\nabla}_{y'}$ on **N** representing the x' and y' components of $\boldsymbol{\nabla} n_e$ in the rotating frame may be defined in a manner analogous to those of $\boldsymbol{\Delta}$ in Eq. (A24) and, like $\boldsymbol{\Delta}$, be based on quadratic fits to (x_i', N_{jp+i}) and its nearest neighbors in the x' and y' directions, respectively. These are, respectively,

$$\nabla_{x';u'u} = \frac{p}{4R_0}(\delta_{u'+1,u} - \delta_{u'-1,u}),$$
$$\nabla_{y';u'u} = \frac{p}{4R_0}(\delta_{u'+p,u} - \delta_{u'-p,u}). \tag{A30}$$

[1] T. Intrator, S. Y. Zhang, J. H. Degnan, I. Furno, C. Grabowski, S. C. Hsu, E. L. Ruden, P. G. Sanchez, J. M. Taccetti, M. Tuszewski, W. J. Waganaar, and G. A. Wurden, Phys. Plasmas **11**, 2580 (2004).
[2] S. Zhang, T. P. Intrator, G. A. Wurden, W. J. Waganaar, J. M. Taccetti, R. Renneke, C. Grabowski, and E. L. Ruden, Phys. Plasmas **12**, 052513 (2005).
[3] J. M. Taccetti, T. P. Intrator, G. A. Wurden, S. Y. Zhang, R. Aragonez, P. N. Assmus, C. M. Bass, C. Carey, S. A. deVries, W. J. Fienup, I. Furno, S. C. Hsu, M. P. Kozar, M. C. Langner, J. Liang, R. J. Maqueda, R. A. Martinez, P. G. Sanchez, K. F. Schoenberg, K. J. Scott, R. E. Siemon, E. M. Tejero, E. H. Trask, M. Tuszewski, W. J. Waganaar, C. Grabowski, E. L. Ruden, J. H. Degnan, T. Cavazos, D. G. Gale, and W. Sommars, Rev. Sci. Instrum. **74**, 4314 (2003).
[4] E. L. Ruden, S. Shouyin Zhang, T. P. Intrator, R. Renneke, W. J. Waganaar, F. T. Analla, and T. C. Grabowski, Rev. Sci. Instrum. **77**, 103502 (2006).
[5] W. Lochte-Holtgreven, *Plasma Diagnostics* (AIP, NY, 1995), p. 607.
[6] J. D. Huba, *NRL Plasma Formulary, Revised* (Naval Research Laboratory, NRL/PU/6790-94-265, Washington, DC, 1998), p. 34.
[7] M. Tuszewski, Plasma Phys. Controlled Fusion **26**, 991 (1984).
[8] M. Tuszewski and W. T. Armstrong, Rev. Sci. Instrum. **54**, 1611 (1983).
[9] M. Tuszewski, Nucl. Fusion **28**, 2033 (1988).
[10] K. V. Roberts and J. B. Taylor, Phys. Rev. Lett. **8**, 197 (1962).
[11] Y. Ito, M. Tanjyo, S. Ohi, S. Goto, and T. Ishimura, Phys. Fluids **30**, 168 (1987).
[12] J. P. Freidberg and L. D. Pearlstein, Phys. Fluids **21**, 1207 (1978).
[13] C. E. Seyler, Phys. Fluids **22**, 2324 (1978).
[14] D. S. Harned, Phys. Fluids **26**, 1320 (1983).
[15] S. Shimamura and Y. Nogi, Fusion Technol. **9**, 69 (1986).
[16] S. Y. Zhang, E. M. Tejero, J. M. Taccetti, G. A. Wurden, T. P. Intrator, W. J. Waganaar, and R. Perkins, Rev. Sci. Instrum. **75**, 4289 (2004).
[17] D. J. Rej, D. P. Taggart, M. H. Baron, R. E. Chrien, R. J. Gribble, M. Tuszewski, W. J. Waganaar, and B. L. Wright, Phys. Fluids B **4**, 1909 (1992).
[18] S. Zhang, G. A. Wurden, T. P. Intrator, E. L. Ruden, W. J. Waganaar, C. T. Grabowski, and J. H. Degnan, IEEE Trans. Plasma Sci. **12**, 223 (2006).
[19] T. Asai, T. Takahashi, T. Kiguchi, Y. Matsuzawa, and Y. Nogi, Phys. Plasmas **13**, 072508 (2006).
[20] E. V. Belova, R. C. Davidson, H. Ji, M. Yamada, C. D. Cothran, M. R. Brown, and M. J. Schaffer, Nucl. Fusion **46**, 162 (2006).
[21] W. T. Armstrong, R. K. Linford, D. A. Platts, and E. G. Sherwood, Phys. Fluids **24**, 2068 (1981).
[22] T. Minato, M. Tanjyo, S. Okada, Y. Ito, M. Kako, S. Ohi, S. Goto, T. Ishimaru, H. Ito, Y. Nogi, S. Shimamaru, Y. Osanai, K. Saito, K. Yokoyama, S. Shiina, S. Hamada, H. Yoshimura, Y. Aso, C. H. Wu, S. Himeno, M. Okamoto, and K. Hirano, *Proceedings of the 9th International Conference on Plasma Physics and Controlled Nuclear Fusion Research*, Baltimore, MD, 1982 (IAEA, Vienna, Austria, 1983), IAEA-CN-41/M-3, Vol. II.
[23] M. Anton, H. Weisen, M. J. Dutch, W. von der Linden, F. Buhlmann, R. Chavan, B. Marletaz, P. Marmillod, and P. Paris, Plasma Phys. Controlled Fusion **38**, 1849 (1996).
[24] W. H. Press, B. P. Flannery, S. A. Teukolsky, and W. T. Vetterling, *Numerical Recipes* (Cambridge University Press, NY, 1986).
[25] G. H. Golub and C. F. Van Loan, *Matrix Computations* (Johns Hopkins University Press, NY, 1983).

Downloaded 18 Dec 2006 to 129.238.237.96. Redistribution subject to AIP license or copyright, see http://pop.aip.org/pop/copyright.jsp